

Fast and slow rotators in the densest environments: a FLAMES/GIRAFFE IFS study of galaxies in Abell 1689 at $z=0.183$

F. D'Eugenio^{1*}, R. C. W. Houghton¹, Roger L. Davies¹ and E. Dalla Bontà^{2,3}

¹*Sub-department of Astrophysics, Department of Physics, University of Oxford, Denys Wilkinson Building, Keble Road, Oxford OX1 3RH*

²*Dipartimento di Fisica e Astronomia "G. Galilei", Università degli Studi di Padova, Vicolo dell'Osservatorio 3, I-35122, Padova, Italy*

³*INAF Osservatorio Astronomico di Padova, Vicolo dell'Osservatorio 5, I-35122, Padova, Italy*

2 October 2018

ABSTRACT

We present FLAMES/GIRAFFE integral field spectroscopy of 30 galaxies in the massive cluster Abell 1689 at $z = 0.183$. Conducting an analysis similar to that of ATLAS^{3D}, we extend the baseline of the kinematic morphology-density relation by an order of magnitude in projected density and show that it is possible to use existing instruments to identify slow and fast rotators beyond the local Universe. We find 4.5 ± 1.0 slow rotators with a distribution in magnitude similar to those in the Virgo cluster. The overall slow rotator fraction of our Abell 1689 sample is 0.15 ± 0.03 , the same as in Virgo using our selection criteria. This suggests that the fraction of slow rotators in a cluster is not strongly dependent on its density. However, within Abell 1689, we find that the fraction of slow rotators increases towards the centre, as was also found in the Virgo cluster.

Key words: galaxies: kinematics and dynamics, galaxies: clusters: individual: Abell 1689

1 INTRODUCTION

1.1 Galaxies and environment density

Early type galaxies (ETGs), despite having masses and luminosities that span several orders of magnitude, obey a number of tight phenomenological laws. These, collectively known as “scaling relations”, include the color-magnitude diagram (CMD; Baum 1959; Visvanathan & Sandage 1977; Sandage & Visvanathan 1978a,b), the color- σ and $Mg - \sigma$ (Burstein et al. 1984; Bender et al. 1993) relations and the fundamental plane (Dressler et al. 1987; Djorgovskii & Davis 1987). With their remarkably small scatter, they impose strong constraints on the structure and evolution of ETGs. Morphologically, ETGs are either classified as ellipticals (Es) or lenticular (S0) galaxies. In the late 1980s, based on new and more accurate spectroscopy, Es were divided into two groups: pressure supported and rotation supported (Bender et al. 1989). It is thus particularly interesting to investigate how such dynamically distinct systems formed and evolved while still obeying the very same scaling relations. Environment certainly plays a major role in galaxy evolution, as witnessed by the morphology-density relation (Dressler 1980): systems in denser surroundings are more likely to be ETGs.

The advent of integral field spectroscopy (IFS) has brought a wealth of information to the field. The SAURON survey discovered the existence of two kinematically distinct classes of ETGs, slow and fast rotators (SR and FR, Emsellem et al. 2007; Cappellari et al. 2007). The former are systems with little to

no rotation, often exhibiting kinematically decoupled cores and misalignment between kinematics and photometry. The latter are flattened systems, compatible with rotational symmetry, where ordered, large scale rotation is important for the gravitational equilibrium. While overlapping with the existing dichotomy among ETGs, the new classification crucially crosses the boundary between Es and S0s, in that FRs populate both morphological classes. Indeed ATLAS^{3D} (the volume limited follow-up survey to SAURON, Cappellari et al. 2011a; Emsellem et al. 2011), found that many morphological Es are FRs. They suggest a new classification paradigm based on kinematics rather than morphology (Cappellari et al. 2011b).

ATLAS^{3D} also presented the kinematic morphology-density relation (kT- Σ), linking the fraction of SRs (f_{SR}) with the local number density of galaxies. f_{SR} is insensitive to environment density over 5 orders of magnitude, with a sharp increase observed only in the inner core of the Virgo cluster. Cappellari et al. (2011b) conclude by asking what would be measured in the denser environments beyond the local Universe: does the fraction of slow rotators increase further or does it stay constant?

Addressing this question would give further insight on the processes that drive galaxy formation and evolution, and is indeed the goal of this work.

1.2 This study

We exploited the unique capabilities of the FLAMES/GIRAFFE multiplexed integral field spectrograph (Pasquini et al. 2002) at the

* E-mail: Francesco.D'Eugenio@physics.ox.ac.uk

Very Large Telescope (VLT) to investigate internal kinematics of galaxies in the dense environment, so to extend the density baseline of the kT - Σ relation. After describing the observations in Section 2, we present the data reduction and analysis in Section 3. The results are presented in Section 4, followed by their discussion in Section 5 and a summary in Section 6.

2 OBSERVATIONS

2.1 Sample selection

Abell 1689 is a massive galaxy cluster at redshift $z = 0.183$ (Struble & Rood 1999). Its regular, concentric X-ray contours suggest it is a relaxed system (Lemze et al. 2008). An X-ray luminosity of $L_X = 20.74 \times 10^{44} \text{ erg s}^{-1}$ makes it considerably more luminous than Coma, which has $L_X = 7.21 \times 10^{44} \text{ erg s}^{-1}$ (Ebeling et al. 1996) and Virgo $L_X = 8.3 \times 10^{43} \text{ erg s}^{-1}$ (Böhringer et al. 1994). Assuming 7-yr *Wilkinson Microwave Anisotropy Probe* Cosmology (Komatsu et al. 2011, $\Omega_m = 0.27, \Omega_\Lambda = 0.73, h_0 = 0.71$) its comoving distance is 741 Mpc, giving $1''$ per 3.0 kpc, so that GIRAFFE deployable integral field units (see below) sample up to $1 R_e$ for most galaxies. GIRAFFE permits the observer to target 15 objects simultaneously and we chose to target 30 galaxies as a compromise between sample size and integration time. Our selection was based on a catalogue from Halkola et al. (2006), and in order to gain the maximum possible signal-to-noise ratio (SNR), we initially selected the 30 ETGs with the highest surface brightness within R_e (including the brightest cluster galaxy). This sample was then subject to two practical constraints. We needed all of our targets to have high resolution HST imaging, which limited our choice to candidates in the innermost regions of the cluster. Physical constraints from the instrument (see Section 2.3) ruled out some targets in the most crowded regions, forcing us to re-select from a reserve list. This left us with 29 galaxies inside the HST field of view and one outside (galaxy 20).

2.2 Archival data.

We used F625W band imaging from the HST Advanced Camera for Surveys, combined with g' and r' band GEMINI imaging. See Houghton et al. (2012) for a thorough description of these data.

2.3 VLT data

We present new data taken with the FLAMES/GIRAFFE spectrometer at the VLT Unit Telescope 2. The L612W filter gives a resolution R of 11800 (the minimum allowed on the instrument) with a wavelength range of 5732-6515 Å (4858-5521 Å in the rest frame), which includes prominent absorption features of old stellar populations (for comparison, SAURON has a wavelength range of 4800-5380 Å). The observations were carried out between 24 May 2009 and 29 May 2009, as detailed in Table 1, which also contains the observing conditions. The instrument provides 30 independent integral field units (IFUs), deployable anywhere on the focal plane. These are arranged in two positioner plates, each hosting 15; each deployable IFU is positioned by a magnetic button, with an accuracy better than $0.08''$ and contains an array of 20 square microlenses, each with a side of $0.52''$ on the sky. They are arranged in 4 rows of 6 (with 4 “dead” corners) for a total field of view of $3'' \times 2''$. Each lenslet is then connected to the spectrometer with

Table 1. A summary of the VLT/FLAMES GIRAFFE/IFU spectroscopy. The seeing was measured on site using telescope guide stars.

| Frame | Plate | Date D/M/Y | night | Time min | Seeing arcsec |
|-------|-------|---------------|-------|-------------|------------------|
| 1 | 1 | 24 May 2009 | 1 | 120 | 0.60 |
| 2 | 1 | 25 May 2009 | 1 | 120 | 0.60 |
| 3 | 1 | 25 May 2009 | 2 | 120 | 0.60 |
| 4 | 1 | 26 May 2009 | 2 | 120 | 0.60 |
| 5 | 1 | 27 May 2009 | 3 | 120 | 0.60 |
| 6 | 2 | 25 May 2009 | 1 | 120 | 0.50 |
| 7 | 2 | 26 May 2009 | 3 | 120 | 0.60 |
| 8 | 2 | 27 May 2009 | 3 | 120 | 0.60 |
| 9 | 2 | 27 May 2009 | 4 | 120 | 0.80 |
| 10 | 2 | 28 May 2009 | 4 | 120 | 0.65 |

a dedicated optical fibre. Alongside the 15 IFUs, each positioner plate also houses 15 sky fibres. These are fully deployable just like the former but carry only one lenslet.

Since the magnetic buttons are larger ($10''$) than the IFU field of view, they cannot be deployed closer than a minimum distance of $11''$ thus constraining the sample selection: galaxies closer than $11''$ on the sky must be allocated on different plates, if at all. As a result, some targets lying in the most crowded regions of the cluster were omitted. We proceeded to divide the sample in two equal sets, with galaxies numbers 1 to 15 assigned to plate 1 and galaxies numbers 16 to 30 to plate 2. Each plate was exposed 5 times for 2 hours, for a total of 10 hours exposure time per galaxy.

We remark that, as detailed in Table 1, the seeing was comparable to the size of the lenslets ($0.52''$). This reduces the correlation between adjacent spaxels.

3 DATA

3.1 Data reduction

We extracted the spectra using the standard ESO pipeline¹, following the guidelines ESO offers².

Each morning the telescope produces a number of calibration frames, including bias, lamp flats and arc lamp frames. To extract the spectra from the raw images we used the closest calibration available. The pipeline is organized into 9 “recipes”, distinct applications with a number of user configurable parameters: we used the default values unless otherwise stated.

For each night we created a master bias out of the 5 raw frames provided. We used the method *ksigma* and the recipe *gimasterbias*, with the keywords *ksigma.low* and *ksigma.high* set to 3.0 to remove cosmic rays.

We then proceeded to “fibre localization”, (tracing the spectra on the chip). This is done using a set of 3 very high SNR lamp flat frames, in the recipe *gimasterflat*. At each spectral pixel on the frame the recipe determines the locations, in the cross-dispersion direction, of the light peaks corresponding to the centres of each fibre signal. A curve is fitted to each profile, and is stored as the trace shape. We used the standard unweighted summation to extract the spectra (we set the keyword *extraction.method* to *SUM*). We set to *PROFILE+CURVE* the keyword *biasremoval.method*, as advised by ESO on the website, while the keywords *fibres.spectra* and *fibres.nspectra* were modified to take into account the occurrence of both broken and unused fibres. The manual indicates that, using *SUM*, the contamination between neighboring spectra is less than 10% of the counts. The recipe also determines the pixel-to-pixel variation corrections and the fibre-to-fibre transmission variations. The wavelength calibration was done separately for each night using the recipe *giwavecalibration*. The resulting wavelength solution has an accuracy of $0.009 \pm 0.033 \text{ \AA}$ and a resolution FWHM of $0.61 \pm 0.07 \text{ \AA}$. The science extraction was performed using *giscience*. We set the parameters *biasremoval.method* to *PROFILE+CURVE* and *flat.apply* to *TRUE*.

3.2 Data analysis

3.2.1 Photometry

We used g' and r' band Gemini imaging to create a catalogue of all galaxies in the observed region of the sky (Houghton et al. 2012). We applied cuts at $r' = 22$ and in the related error ($\sigma_{r'}, \sigma_{g'} < 0.1$ mag). The resulting catalogue has been used to compute the number density of galaxies (Section 4.3), the cluster Luminosity Function (LF) (Section 5.1) and the cluster CMD (Section 5.1.1). HST imaging was used to determine de Vaucouleurs (de Vaucouleurs 1953) effective radii R_e (using the curve of growth method of Houghton et al. 2012) and ellipticities ϵ , whenever this was possible. In practice one galaxy (number 20 in Table 2) lies partially outside the ACS field of view, and takes its photometric parameters from the r' Gemini image.

Since a large fraction of our sample is found in very dense regions, the surface photometry is often contaminated by that of a neighbour. Consequently the R_e values in Table 2 include a quality flag Q, as in Houghton et al. (2012).

Following Cappellari et al. (2007) we adopted the method

of moments to determine ellipticities: after identifying the image isophotes we compute, for each of them, the position angle of the major axis PA, the ellipticity ϵ and the surface area A . The ellipticity of the k -th isophote ϵ_k is defined by

$$(1 - \epsilon_k^2) \equiv \frac{\sum_{i \in \mathcal{I}_k} F_i y_i}{\sum_{i \in \mathcal{I}_k} F_i x_i} \quad (1)$$

where F_i is the flux associated with the i -th pixel, and the coordinates (x, y) are drawn from the galaxy centre, with the x -axis along the photometric major axis. The sum is conducted on the set of all pixels comprised in the k -th isophote. We associate to each isophote an ellipse of area A_k equal to the isophote area, ellipticity ϵ_k and position angle PA_k , and associate to it a radius defined by $R_k \equiv \sqrt{A_k/\pi}$. SAURON and ATLAS^{3D} based their classification on values computed at $1 R_e$. We therefore define ϵ_e as the value of ϵ_k computed within the isophote of associated radius R_e . The results are listed in Table 2. We find them to be robust against changes in R_e , except for galaxy number 9 (Table 2), which exhibits peculiar photometry, having an abrupt change in both ϵ and position angle at a radius of $\approx 0.5''$.

3.2.2 Stellar kinematics

Stellar kinematics were extracted using pPXF, a penalized maximum likelihood algorithm developed by Cappellari & Emsellem (2004). It fits the line-of-sight velocity distribution (LOSVD) in pixel space, by convolving a linear combination of stellar template spectra with an LOSVD expressed by the truncated Gauss-Hermite series (van der Marel & Franx 1993; Gerhard 1993):

$$\mathcal{L}(v) = \frac{e^{-(1/2)y^2}}{\sigma\sqrt{2\pi}} \left[1 + \sum_{m=3}^M h_m H_m(y) \right] \quad (2)$$

where $y = (v - V)/\sigma$ and the H_m are Hermite polynomials. In practice however, our SNR was mostly lower than that (≈ 60) required to reliably measure the weights h_3 and h_4 so we fitted a Gaussian function, obtaining just V and σ in the above expression. While ATLAS^{3D} team used MILES stellar template library (Sánchez-Blázquez et al. 2006), its FWHM resolution of 2.54 \AA (Beifiori et al. 2011) was lower than that of our data (see Section 3.1), so we used the high resolution version ($R = 40000$) of the ELODIE template library (Prugniel & Soubiran 2001), with FWHM of 0.13 \AA . The two libraries span similar regions in the age-metallicity space; MILES reaches lower ages ($\approx 7 \text{ Gyr}$ vs $\approx 8 \text{ Gyr}$) and includes some old, metal poor stars ($Z \approx 1/100 Z_\odot$), but these are not relevant when fitting ETGs, and the change of library is unlikely to introduce any significant bias when compared to ATLAS^{3D} measurements. All ELODIE templates have a gap at $\lambda \approx 5414 \text{ \AA}$, so we cut the galaxy spectra at 5300 \AA . For each galaxy we computed a weighted average (with sigma clipping rejection) of all the 20 spectra, and fed it to pPXF along with all the templates available in ELODIE. This resulted in ≈ 15 templates being selected for each galaxy, and we use this subset to fit the individual fibre spectra of the galaxy. We used formal errors derived by pPXF (we did not exploit the penalizing functionality of the algorithm). These are typically of the order of 15 km s^{-1} for V and 17 km s^{-1} for σ , but they do not take into account the correlation introduced when log-rebinning.

¹ <http://www.eso.org/sci/software/pipelines/giraffe/giraf-pipe-recipes.html>

² <ftp://ftp.eso.org/pub/dfs/pipelines/giraffe/giraf-manual-2.8.7.pdf>

Table 2. Our sample of 30 bright galaxies in Abell 1689.

| Galaxy | Halkola | RA | DEC | M_K | R_e | Q | ϵ_e | PA | p(SR) | $\lambda_R(IFU)$ | $\log \Sigma_3$ |
|--------|---------|-----------|----------|--------|------------------|-------|--------------|------|-------|-------------------|----------------------|
| (1) | (2) | (deg) | (deg) | (mag) | (arcsec) | (1-3) | (8) | (9) | (0-1) | (11) | (Mpc ⁻²) |
| (3) | (4) | (5) | (6) | (7) | (8) | (9) | (10) | (11) | (12) | | |
| 1 | 17 | 197.94862 | -1.15575 | -23.28 | 0.65 ± 0.29 | 2 | 0.286 | 20 | 0.02 | 0.412 ± 0.092 | 2.381 |
| 2 | 3 | 197.94831 | -1.14250 | -23.16 | 1.27 ± 0.57 | 1 | 0.583 | 163 | 0.00 | 0.585 ± 0.053 | 2.408 |
| 3 | 12 | 197.95400 | -1.13998 | -23.57 | 0.71 ± 0.32 | 2 | 0.363 | 47 | 0.00 | 0.611 ± 0.087 | 2.279 |
| 4 | 34 | 197.96433 | -1.14525 | -22.58 | 1.15 ± 0.51 | 2 | 0.032 | 235 | 0.00 | 0.455 ± 0.105 | 2.333 |
| 5 | 22 | 197.96239 | -1.15608 | -24.97 | 2.84 ± 1.24 | 2 | 0.219 | 113 | 0.00 | 0.252 ± 0.022 | 2.928 |
| 6 | 47 | 197.96764 | -1.16323 | -25.41 | 2.39 ± 1.04 | 2 | 0.330 | 266 | 0.91 | 0.116 ± 0.022 | 3.083 |
| 7 | 65 | 197.97640 | -1.15380 | -22.99 | 0.85 ± 0.38 | 2 | 0.108 | 311 | 0.02 | 0.352 ± 0.100 | 2.339 |
| 8 | 31 | 197.95769 | -1.17172 | -24.86 | 2.74 ± 1.20 | 3 | 0.090 | 196 | 0.40 | 0.080 ± 0.026 | 3.468 |
| 9 | 38 | 197.95643 | -1.17477 | -24.28 | 7.51 ± 3.28 | 3 | 0.077 | -41 | 0.00 | 0.428 ± 0.030 | 3.748 |
| 10 | 43 | 197.95238 | -1.18489 | -23.87 | 1.69 ± 0.74 | 2 | 0.049 | -157 | 0.37 | 0.158 ± 0.046 | 2.658 |
| 11 | 37 | 197.94754 | -1.18383 | -22.75 | 0.74 ± 0.33 | 2 | 0.217 | -41 | 0.00 | 0.510 ± 0.096 | 2.489 |
| 12 | 32 | 197.95437 | -1.17140 | -26.18 | 13.92 ± 6.08 | 3 | 0.149 | -62 | 0.95 | 0.037 ± 0.024 | 3.607 |
| 13 | 14 | 197.94564 | -1.16432 | -23.64 | 1.58 ± 0.69 | 2 | 0.107 | 44 | 0.06 | 0.214 ± 0.049 | 2.696 |
| 14 | 6 | 197.94071 | -1.16265 | -23.48 | 0.62 ± 0.28 | 2 | 0.361 | 88 | 0.03 | 0.444 ± 0.093 | 2.582 |
| 15 | 2 | 197.93615 | -1.15561 | -22.81 | 0.93 ± 0.42 | 2 | 0.029 | 83 | 0.00 | 0.356 ± 0.095 | 2.130 |
| 16 | 7 | 197.94359 | -1.15721 | -23.63 | 1.81 ± 0.79 | 2 | 0.138 | 0 | 0.00 | 0.257 ± 0.043 | 2.779 |
| 17 | 20 | 197.95362 | -1.15161 | -23.04 | 0.46 ± 0.21 | 2 | 0.558 | 138 | 0.00 | 0.505 ± 0.092 | 2.285 |
| 18 | 41 | 197.96484 | -1.15373 | -23.55 | 0.95 ± 0.42 | 2 | 0.174 | 198 | 0.00 | 0.410 ± 0.094 | 2.830 |
| 19 | 35 | 197.96782 | -1.15578 | -25.13 | 2.27 ± 0.99 | 2 | 0.246 | 180 | 0.76 | 0.136 ± 0.026 | 3.321 |
| 20 | - | 197.98916 | -1.15270 | -24.38 | 1.55 ± 0.19 | 2 | 0.040 | 98 | 0.00 | 0.171 ± 0.064 | 2.061 |
| 21 | 69 | 197.97680 | -1.16486 | -22.56 | 0.52 ± 0.23 | 2 | 0.278 | 278 | 0.00 | 0.439 ± 0.107 | 2.504 |
| 22 | 75 | 197.97635 | -1.18002 | -23.47 | 0.86 ± 0.38 | 2 | 0.301 | 193 | 0.00 | 0.626 ± 0.089 | 2.622 |
| 23 | 61 | 197.96103 | -1.17819 | -23.19 | 0.57 ± 0.25 | 2 | 0.055 | 292 | 0.00 | 0.416 ± 0.092 | 2.822 |
| 24 | 70 | 197.96526 | -1.19081 | -23.66 | 1.19 ± 0.52 | 2 | 0.245 | -124 | 0.09 | 0.290 ± 0.055 | 2.411 |
| 25 | 60 | 197.96108 | -1.18797 | -23.64 | 0.85 ± 0.37 | 2 | 0.261 | -41 | 0.00 | 0.509 ± 0.092 | 2.469 |
| 26 | 29 | 197.95675 | -1.17549 | -24.91 | 4.64 ± 2.02 | 3 | 0.116 | -26 | 0.45 | 0.120 ± 0.027 | 3.446 |
| 27 | 42 | 197.95666 | -1.17153 | -24.94 | 3.36 ± 1.47 | 3 | 0.154 | -53 | 0.96 | 0.107 ± 0.029 | 3.660 |
| 28 | 8 | 197.93336 | -1.18330 | -23.54 | 0.83 ± 0.37 | 2 | 0.617 | -35 | 0.00 | 0.588 ± 0.094 | 2.968 |
| 29 | 28 | 197.95005 | -1.17060 | -23.63 | 0.69 ± 0.31 | 2 | 0.081 | 96 | 0.00 | 0.445 ± 0.099 | 3.060 |
| 30 | 4 | 197.93953 | -1.16139 | -23.35 | 0.93 ± 0.41 | 2 | 0.265 | 70 | 0.03 | 0.370 ± 0.092 | 2.594 |

Note. — Column (1): galaxy ID number used throughout this work. Column (2): galaxy ID from Halkola et al. (2006). Column (3): right ascension in degrees and decimal (J2000.0). Column (4): declination in degrees and decimal (J2000.0). Column (5): K -band galaxy magnitude derived from the apparent r' -band magnitude and corrected as detailed in Section 5. Column (6): R_e obtained with a curve of growth method and masking nearby objects, see Section 3.2.1. Column (7): quality of the R_e determination. A value of 1 is only given to the best fits. Values of 3 are assigned to objects with severe contamination. Column (8): ellipticity determined with the method of moments, inside the isophote of area πR_e^2 . Column (9): position angle determined with the method of moments, inside the isophote of area πR_e^2 . Column (10): probability that the galaxy is a SR, see Fig. 4. Column (11): λ_R measured within the whole IFU field of view. Column (12): Mean surface density of galaxies inside the circle centred on the galaxy and containing its 3 closest neighbours.

Due to the high spectral resolution and low SNR, we decided not to subtract the sky, but rather to fit it simultaneously with the stellar templates. Like Weijmans et al. (2009), we provided pPXF with all the simultaneous sky spectra and let the maximum likelihood algorithm rescale them to best fit the data.

4 RESULTS

4.1 Kinematic maps

The results of the kinematic extraction can be seen on Fig. 1. There are four frames for each galaxy, from left to right: high resolution photometry (from either HST or GEMINI); low resolution GIRAFFE spectrograph photometry; the extracted velocity map and the extracted velocity dispersion map. Above each galaxy we give the ID number; the celestial orientation is given by the black compass arrows (N and E). Corner spaxels and spaxels corresponding to

broken/unused optic fibres are depicted in black. Although the spatial resolution is low, rotation can be clearly seen in some galaxies, while no such features are seen on others.

We cannot detect kinematically decoupled cores (KDCs) and double σ peaks ($2\text{-}\sigma$) as in Krajnović et al. (2011), because our spatial resolution is too coarse. If we try to detect SRs from the velocity maps by eye, we identify at most six: these are galaxies 4, 8, 12, 20, 26 and 27. The overall fraction of SRs in the sample would then be 0.20, in line with what was found in the Virgo core (Cappellari et al. 2011b). However we are subject to contamination from face on discs appearing as SRs, which increases f_{SR} .

We also highlight five more objects which, despite exhibiting large scale rotation, have misaligned kinematic axes, a feature more common in SRs than in FRs (Krajnović et al. 2011): these are galaxies 1, 3, 5, 9, 17 and 25. Galaxies 3 and 17 have very high ellipticities, and are thus unlikely to be SRs. Galaxy 5 has high ve-

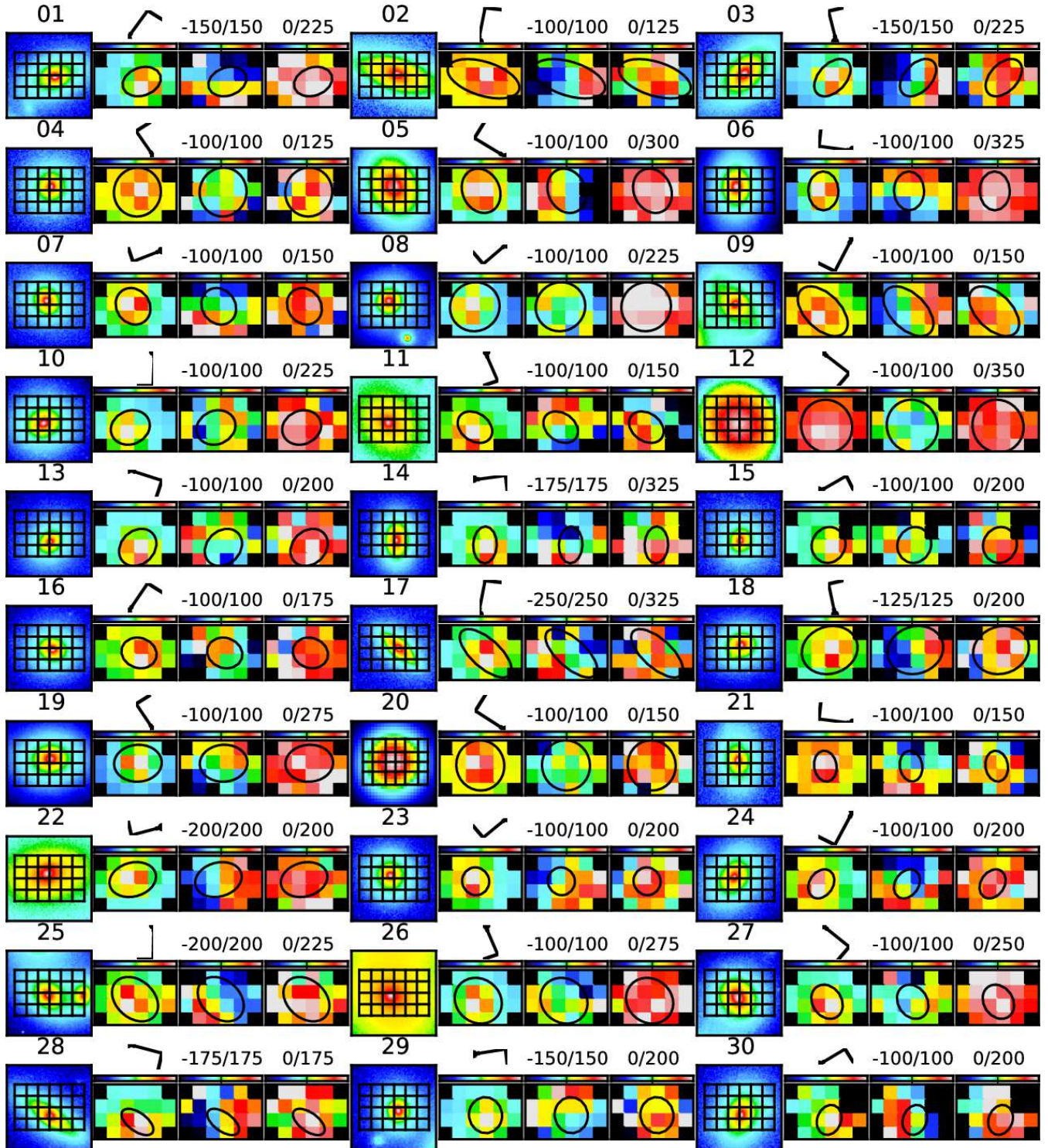


Figure 1. Kinematic maps of the Abell 1689 sample. Each horizontal set of four images depicts one of the 30 galaxies in the sample. The first plot shows HST photometry (apart from target 20). Superimposed is the FLAMES/GIRAFFE footprint. The second plot is the reconstructed image from VLT integral spectroscopy, where each square is a spaxel, corresponding to a lenslet in the instrument. Superimposed is an isophote at either R_e , or the closest fraction that fits into the IFU footprint. The four black corners correspond to unused “dead” corners, while other black spaxels (seen in 11, 15 and 30) correspond to broken or unused fibres. The third and fourth plots depict the kinematic maps: velocity and velocity dispersion. The black compass arrows show North and East. The colorbar limits are given in km s^{-1} .

locity dispersion, and also contains an inner disc ($R = 1.5$ kpc) in the HST imaging.

4.2 λ_R and kinematic classification.

Emsellem et al. (2007) introduced the estimator λ_R to measure the projected specific angular momentum of galaxies and Emsellem et al. (2011) further show how the combination of λ_R and ellipticity ϵ conveniently captures the kinematic boundary between SRs and FRs. λ_R is defined as

$$\lambda_R(I) \equiv \frac{\sum_{i \in I} F_i R_i |V_i|}{\sum_{i \in I} F_i R_i \sqrt{V_i^2 + \sigma_i^2}} \quad (3)$$

where F_i , R_i , V_i and σ_i are the flux, distance from the galaxy centre, velocity and velocity dispersion of the i -th spaxel; the sum is conducted over all spaxels inside some subset I of the IFU footprint. Emsellem et al. (2007, 2011) define $\lambda_R(R_e)$ as the value of λ_R computed inside the ellipse of area πR_e^2 (see Section 3.2.1). In our study however that ellipse may either not comprise enough spaxels to reliably measure $\lambda_R(R_e)$, or be too large to fit inside the IFU footprint. Therefore we used existing SAURON data to estimate how our particular observing setup affects the measured value of λ_R .

4.2.1 Effect of pixelisation on λ_R .

The original SAURON sample covers a wide range of ETGs types (de Zeeuw et al. 2002), and its data is publicly available³. We use it to simulate observations with FLAMES/GIRAFFE, in order to determine how distance and reduced spatial resolution affect measurements of λ_R . For each galaxy we created a kinematic model using kinemetry⁴ (Krajnović et al. 2006); each model was then projected to the distance of Abell 1689 and convolved with a seeing of $0.8''$, before being “observed” with FLAMES/GIRAFFE. We created 10000 realizations of each model, adding Gaussian errors of 15 km s^{-1} and 17 km s^{-1} for V and σ respectively (Section 3.2.2), and proceeded to measure λ_R for each of them.

In their λ_R vs ϵ diagram, Emsellem et al. (2007, 2011) plot values computed on the same SAURON spectrograph images, at the same spatial scale of $1 R_e$. For the small galaxies in our sample however, R_e covers just a few pixels whereas the large galaxies have R_e larger than the field of view of the IFU. For this reason we cannot follow the ATLAS^{3D} prescription precisely. We therefore introduced $\lambda_R(IFU)$, defined as the value of λ_R computed using all the available spaxels in the IFU field of view and show through simulation of the SAURON results that it is a satisfactory proxy for $\lambda_R(R_e)$.

Fig. 2 shows $\Delta\lambda_R$ plotted against R_e , where $\Delta\lambda_R$ is defined as the difference between $\lambda_R(IFU)$ and the value of $\lambda_R(R_e)$ of Emsellem et al. (2007). We can use this information to determine the correction and the uncertainty that we need to apply to $\lambda_R(IFU)$ to obtain $\lambda_R(R_e)$. It is clear how our ability to recover the true value of $\lambda_R(R_e)$ improves with increasing R_e . To make use of this information we separate the sample into three groups, based on R_e (the divisions are at R_e values of $1.15''$ and $1.70''$ which

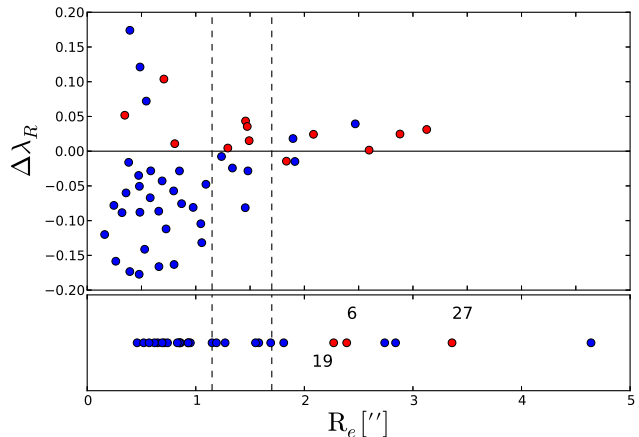


Figure 2. Simulated observation of SAURON data with FLAMES/GIRAFFE, at $z = 0.183$. $\Delta\lambda_R$ is the difference between $\lambda_R(IFU)$ (computed from simulated observations of SAURON data with GIRAFFE) and the value $\lambda_R(R_e)$ given in Emsellem et al. (2007), plotted against R_e . Slow/fast rotators are denoted by red/blue dots, and classified as in Emsellem et al. (2007) (upper panel). In the lower panel we show the values of R_e for our sample of galaxies in Abell 1689, where the symbol colour indicates SRs (red) and FRs (blue), according to a classification done using the λ_R - ϵ plot (Fig. 4), as described in Section 4.2.2. Dashed vertical lines define regions over which we estimate biases and systematic errors (see Section 4.2.1).

naturally divide the Abell 1689 sample and are shown as vertical dashed lines in Fig. 2). We find the following biases (mean offset) and systematic errors (dispersion): for galaxies with $R_e < 1.15''$ $\Delta\lambda_R = -0.06 \pm 0.09$; for galaxies with $1.15'' \leq R_e < 1.7''$, $\Delta\lambda_R = -0.01 \pm 0.04$, and for the remainder, $\Delta\lambda_R = 0.01 \pm 0.02$.

We corrected $\lambda_R(IFU)$ according to the biases measured, summing the systematic errors in quadrature to the random errors. This correction takes into account both the different spatial scale between $\lambda_R(IFU)$ and $\lambda_R(R_e)$ and the different spatial resolution between $\lambda_R(IFU)$ and ϵ_e . In Fig. 3 we plot simulated values of $\lambda_R(IFU)$ against published values of ϵ_e (from Emsellem et al. 2007). Despite the aforementioned differences, there is little (10%) misclassification in our diagram, especially at high values of R_e . We can calculate the probability distribution for the number of SRs (galaxies below the line defined by $0.31 \times \sqrt{\epsilon}$ and the green line in Fig. 3, Emsellem et al. 2011). This is most easily done with a Monte Carlo approach. For each galaxy we assume Gaussian errors in λ_R , truncated so that $0 \leq \lambda_R \leq 1$ and sample 10000 times. The resulting probability distribution is Gaussian-like and we find 12.3 ± 1.7 slow rotators, where the true value is 12. This justifies both our choice of $\lambda_R(IFU)$ to substitute for $\lambda_R(R_e)$, and the use of ϵ computed at a different resolution and radius than $\lambda_R(IFU)$.

4.2.2 λ_R measurements and the statistical calculation of f_{SR}

In Fig. 4 we show the $\lambda_R(IFU)$ vs ϵ_e plot for our Abell 1689 data. Given the simulation in the previous section, the values of $\lambda_R(IFU)$ have been corrected by -0.06 , -0.01 and 0.01 for galaxies with $R_e < 1.15''$, $1.15'' \leq R_e < 1.7''$ and $R_e \geq 1.7''$ respectively. The errors include both the formal random error (from pPXF) and the systematic error (0.09, 0.04 and 0.02 for the three ranges of R_e from the previous simulations). Given these errors we can calculate the probability distribution for the number of SRs, as done previously for the simulated SAURON data. We find 4.5 ± 1.0 slow rota-

³ <http://www.strw.leidenuniv.nl/sauron/>

⁴ The IDL KINEMETRY routine can be found at <http://www.eso.org/~dkrajnov/idl/>

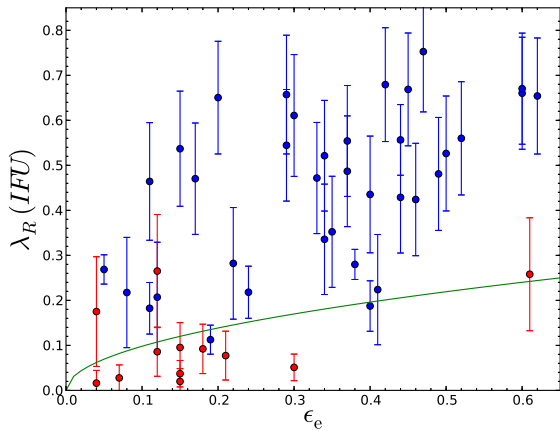


Figure 3. $\lambda_R(IFU)$ vs ϵ_e for our simulated FLAMES/GIRAFFE observations of the SAURON sample of galaxies. The green lines, which separates SRs (below it) from FRs, has equation $\lambda_R = 0.31 \sqrt{\epsilon}$. Red and blue dots denote SRs and FRs respectively, according to the original SAURON classification (Emsellem et al. 2007). While $\lambda_R(IFU)$ has been measured on the redshifted and resampled data, the values of ϵ on the x axis are the original values published in Emsellem et al. (2007). Despite the latter being measured on much higher resolution than $\lambda_R(IFU)$, and at a different radius, the impact on the classification is low. Misclassified galaxies correspond either to red dots above the green line and blue dots below it.

tors, corresponding to $f_{SR}=0.15 \pm 0.03$. Galaxy number 9, which has peculiar photometry and an uncertain value of ϵ_e , has no effect on the result, because its value of $\lambda_R(IFU)$ is greater than ≈ 0.25 (the maximum allowed for any SR) by more than 3σ .

Emsellem et al. (2007) warn about using only λ_R to assign a galaxy to either the slow or fast rotator class. The discrepancy between the “by eye” classification and the classification here bolsters that warning. However, when studying galaxies beyond the local Universe, such a detailed analysis as was done by the ATLAS^{3D} team is unfeasible. We are thus forced to rely on a statistical approach.

4.3 Environment density

For each galaxy in the sample we computed the local environment density following Cappellari et al. (2011b). We defined Σ_3 as the number density inside the circular area centred around the target galaxy and encompassing three other galaxies. Density estimates were done using only valid targets in the catalogue of Section 5.1. We applied a constant field correction of $0.49 \text{ gal arcmin}^{-2}$, measured averaging data from one hundred 1 arcmin^2 fields from SDSS DR7 (Abazajian et al. 2009), without correcting for cluster/groups contamination. For comparison, the minimum value found in our sample is $3.83 \text{ gal arcmin}^{-2}$. In Fig. 5 we show f_{SR} versus Σ_3 ; we compare it to the results of the ATLAS^{3D} survey, and in particular to f_{SR} (Cappellari et al. 2011b). The Virgo core corresponds to the densest bin in ATLAS^{3D}, with $f_{SR} = 0.25$, double that typically found in less dense environments ($f_{SR} \approx 0.12$). We probe environments with values of $\log_{10}\Sigma_3$ between 2.06 and 3.75: the minimum is comparable to the core of Virgo, and the maximum is 1.7 dex higher. In this sense our work starts exactly where ATLAS^{3D} finished. We find a sharp increase in f_{SR} with projected density, ranging from $f_{SR}=0.01$ in the least dense environment to $f_{SR}=0.58$ in the densest environment. Errors due to misclassification, albeit

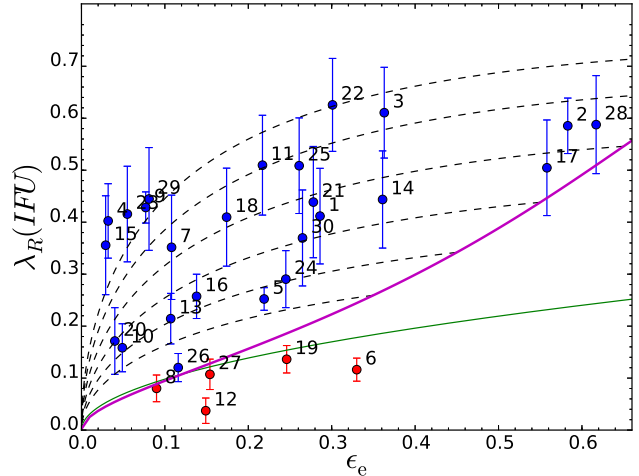


Figure 4. $\lambda_R(IFU)$ vs ϵ_e for all target galaxies in Abell 1689. The green line has equation $\lambda_R = 0.31 \sqrt{\epsilon}$ and separates fast rotators (blue dots above it) from slow rotators (red dots below it). Error bars are dominated by the systematic error (Section 4.2.2). Notice that we corrected the measured value of $\lambda_R(IFU)$ by subtracting -0.06 , -0.01 and 0.01 , depending on R_e for each galaxy (see again Section 4.2.2). The solid magenta line represents the edge-on view of axisymmetric galaxies with $\beta = 0.70 \times \epsilon$, while the black dashed lines represent the trajectories of 6 of these galaxies (with $\epsilon = 0.85, 0.75, \dots, 0.35$) as their viewing angle goes from edge-on (on the magenta line) to face on (towards the origin). For more information on how these models were constructed see Emsellem et al. (2011)

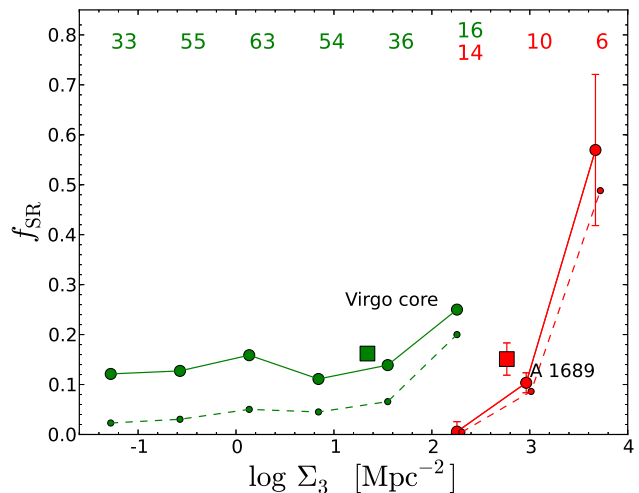


Figure 5. Fraction of slow rotators f_{SR} over the ETGs population in ATLAS^{3D}, including Virgo cluster (green circles, solid green line), as given in Cappellari et al. (2011b), and fraction of slow rotators in our sample of Abell 1689 galaxies (red circles, solid red line). Numbers at the top are the total number of galaxies in that bin, with the same color code. The error bars for the Abell 1689 points represent the uncertainty in the slow rotators classification, as estimated in Section 4.2.2. The green square is the value of f_{SR} that we measure resampling Virgo using our sample luminosity function. The error bars are smaller than the marker size. The red square is the average fraction of slow rotators found in our sample. The lower, smaller circles and dashed lines are the fractions computed with respect to the total cluster population, for ATLAS^{3D} (green) and Abell 1689 (red); this is an estimate based on spirals and blue ellipticals counts.

large, show that the densest bin in Abell 1689 has a higher fraction of SRs than Virgo core (Fig. 5). The intermediate bin has a value of f_{SR} compatible, within the errors, with both the field-group environments and overall Virgo cluster value but is however lower than the Virgo core. f_{SR} in the least dense bin is lower than ATLAS^{3D} field and group values.

However, considering the whole Abell 1689 sample, we find for an average value of $\log_{10}\Sigma_3 = 2.77$ that the SR fraction is 0.15 ± 0.03 (red square in Fig. 5), which is the same as the overall SR fraction in the Virgo cluster, when sampled in the same way (green square). Furthermore, both values are similar to the field and group samples in ATLAS^{3D}, suggesting little to no difference in f_{SR} when it is averaged over the whole cluster.

5 DISCUSSION

5.1 Sample selection effects

In order to assess the robustness of our result, it is important to study the relation between the sample of 30 galaxies and its parent population. Our sample selection, limited by both observing and instrument constraints, biases our study in different ways. In this section we discuss how these effects change f_{SR} .

Having in mind the ATLAS^{3D} study of the Virgo cluster as a point of comparison, we determined the Abell 1689 K-band LF. We took the r' -band catalogue (Section 3.2.1) and, following Houghton et al. (2012), applied a k-correction to the GMOS r' -band magnitudes. The results have been converted to K_s band (and Vega system), using Maraston (2005) models, where we assumed an age of 10.4 Gyr (Houghton et al. 2012) and passive evolution. We finally applied a cut at $M_K = -21.5$ mag, thus matching ATLAS^{3D} parent sample selection. The result is shown in Fig. 6 (blue circles), where we compare it with the cluster RS (as determined by Houghton et al. 2012, red diamonds) and our sample (yellow squares). The Virgo ETG LF is also plotted (green triangles).

Knowing the K-band magnitudes of our sample, we can show f_{SR} as a function of magnitude. In Fig. 7, the value of f_{SR} observed in our sample (red) is compared to the fraction of SRs over the ETGs population of Virgo (green). The two are, within the errors, remarkably similar; however we do not reach magnitudes beyond ≈ -23 mag to probe the faint SRs.

5.1.1 Red sequence bias

Our sample falls entirely on the red sequence (RS), a property that was not sought after. We know that the RS does not necessarily trace the morphological ETGs population, as it can include red spirals and omit blue ellipticals. How many ETGs lying off the RS have we left out of our sample? A rich, relaxed cluster like Abell 1689 comprises a very small fraction of spirals, particularly in the core. In fact the ratio between the RS LF and the cluster LF goes from 1 at the bright end to 0.70 at $M_K = -22.5$ mag. This means that including 10 “blue” galaxies in the faintest magnitude bins would remove the RS bias, leaving us with a color “fair” sample. These faint galaxies are more likely to be FRs (Fig. 7), so the bias introduced by selecting galaxies on the RS leads us to overestimate f_{SR} . In fact, if we assume that these ten galaxies are all FRs, and that they are distributed spatially much like the observed targets, we can determine the kinematic morphology-density relation for an unbiased sample (with respect to color) which we show in

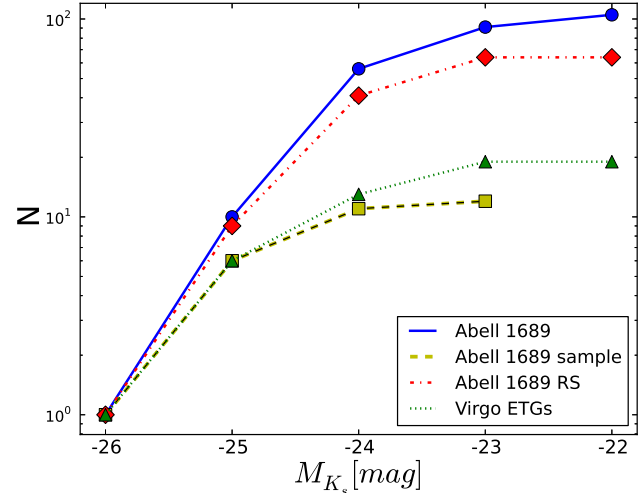


Figure 6. Abell 1689 (blue circles) and sample (yellow squares) K-band LFs, obtained from GEMINI/GMOS g' band and r' band imaging. r' band magnitudes have been converted to M_{K_s} band as described in Section 5. Red diamonds trace the cluster RS, as determined by Houghton et al. (2012). Green triangles represent Virgo ETGs LF, from ATLAS^{3D} survey (data available at www-astro.physics.ox.ac.uk/atlas3d/)

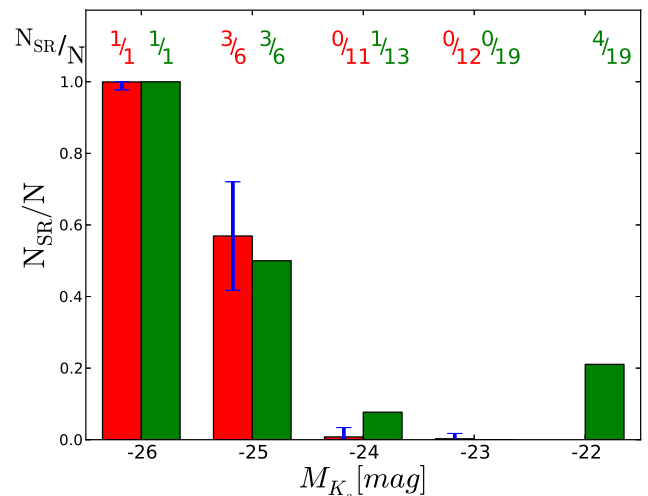


Figure 7. Fraction of SRs for Abell 1689 sample (red histogram) and in Virgo ETGs (green), as a function of magnitude. The number of SRs and the total number of galaxies in each magnitude bin are given at the top. For Abell 1689 the number of SRs has been rounded off. (Section 4.2.2).

Fig. 5 (smaller red dots and red dashed line), with the relation from ATLAS^{3D} (smaller green dots and green dashed line). The good overlap between ETGs and the RS in Abell 1689 causes f_{SR} to stay the same, whether the fraction is computed against the RS or overall galaxy population. This is not true in a less relaxed, spiral rich cluster like Virgo (Fig. 5).

5.1.2 Magnitude selection

We know that in Virgo, f_{SR} varies as a function of M_K (Fig. 7), and that the LFs of Virgo and Abell 1689 are different, in that Virgo is relatively richer in brighter objects (Fig. 6). Since our sample is not fully representative of the Abell 1689 population, what bias does

this introduce in the measured value of f_{SR} ? A rigorous answer to this question is impossible, because we do not know if the SR LF varies as a function of redshift and/or environment. In particular, Virgo is a small and dynamically young cluster, whereas Abell 1689 is a massive, relaxed system. However, using a simulation, we can estimate what SR fraction we would measure in Virgo with the same selection effects present in our Abell 1689 sample.

Let us assume that the SR fraction as a function of magnitude is the same in Abell 1689 and Virgo (reasonable given Fig. 7) and that the galaxies were selected only on their magnitude and no other properties (not true, as discussed in Section 2.1, but reasonable given the substitutions required to comply with proximity constraints). Using the actual Abell 1689 LF, we drew random subsamples from the ATLAS^{3D} Virgo ETG population. These samples yielded $f_{\text{SR}} = 0.16 \pm 0.01$, in agreement with the actual Virgo value of 0.16. Thus despite being biased towards brighter galaxies, we should measure the same f_{SR} ; this is because we sample down to, but not including, the faintest magnitude bin of ATLAS^{3D}, where f_{SR} suddenly increases.

5.1.3 Other factors

We remark that the distribution of projected ellipticities ϵ_e of our sample is different from that observed in Virgo. Since the former is richer in round objects, and since SRs generally appear rounder, it follows that our sample could be biased towards higher values of f_{SR} . It may well be that the clusters ϵ distributions are different, in which case a higher fraction of round objects may increase f_{SR} .

Another possible source of bias is the intrinsic shape of Abell 1689: according to Oguri et al. (2005) and Corless et al. (2009), Abell 1689 is elongated along the line of sight, so that its measured Σ_3 is higher than what we would observe from another point of view. If the cluster length along the line of sight direction were γ times longer than the diameter of the sky projection, then the value of Σ_3 observed would be $\approx \gamma$ times the unbiased value. Since the maximum reasonable value of γ is ≈ 3 , in Fig. 5 $\log \Sigma_3$ is overestimated by at most ≈ 0.5 , which does not significantly affect our results.

Finally we remark that the corrections to $\lambda_R(\text{IFU})$ that we derived in Section 4.2.1 increase f_{SR} ; had we applied no correction, we would have 3.8 ± 1.0 SRs, so an even lower value of f_{SR} .

5.2 General remarks

Abell 1689 has a higher average density than Virgo, but the same value of f_{SR} . Inside the cluster, in agreement with the findings of Cappellari et al. (2011b), f_{SR} rises with projected density. In the least dense region f_{SR} is smaller than the ATLAS^{3D} field/group value. Given the low number of galaxies per bin, we cannot rigorously claim that this is representative. However, a similar ‘‘depletion’’ is observed in the outskirts of Virgo cluster (Cappellari et al. 2011b). One explanation could be that massive SRs are driven by dynamical friction towards the centre of the cluster. If these were originally distributed in the cluster like other galaxies, dynamical friction would reduce their orbital velocity and radius. Since this process is more effective on more massive galaxies, it would concentrate SRs (more massive on average) with respect to other galaxies.

6 SUMMARY

We demonstrated the use of FLAMES/GIRAFFE in IFU mode to perform a survey of 30 galaxies in Abell 1689 at $z = 0.183$. The data has sufficient quality and spatial resolution to classify the majority of targets as either SRs or FRs. In summary:

(i) we find, in agreement with ATLAS^{3D} results, that SRs populate the high luminosity end of the LF; the SR LFs measured from the Virgo ATLAS^{3D} sample and our Abell 1689 sample are identical down to $M_K = -23$ mag.

(ii) the fraction of slow rotators in our sample is $f_{\text{SR}}=0.15 \pm 0.03$. If we apply the same selection criteria to all Virgo galaxies in ATLAS^{3D}, we find the same fraction (assuming that the distribution of SRs with magnitude is the same in both clusters). This indicates that f_{SR} is not affected by the average number density of the cluster. Both Abell 1689 and Virgo average f_{SR} are in line with the ATLAS^{3D} value for field and group environments.

(iii) the fraction of SRs increases towards the denser, central region of the cluster. This is in agreement with what was found in Virgo, where SRs concentrate in the cluster core. This could be a consequence of dynamical friction, as SRs dominate the high mass end of the galaxy population.

It is important to expand this study, both to further study Abell 1689 down to lower luminosities and increase the number of observed clusters, to quantify the scatter in f_{SR} .

ACKNOWLEDGMENTS

We thank Michele Cappellari and John Magorrian for their helpful comments and suggestions. We are particularly grateful to the referee Eric Emsellem, whose comments significantly improved this paper. We wish to express our thanks to Jonathan Smoker, who was instrument scientist for FLAMES when we took the observations. FDE acknowledges support from the Physics Department, University of Oxford and travel support from Merton College, Oxford. RLD acknowledges travel and computer grants from Christ Church College, Oxford, and support from the Royal Society in the form of a Wolfson Merit Award 502011.K502/jd. RLD also acknowledges the support of the ESO Visitor Programme which funded a 3-month stay in 2010.

EDB was supported by the grants CPDA089220/08 and 60A02-5934/09 of Padua University, and ASI-INAF I/009/10/0 of Italian Space Agency, and by a grant of Accademia dei Lincei and Royal Society. EDB acknowledges the Sub-department of Astrophysics, Department of Physics, University of Oxford and Christ Church College for the hospitality while this paper was in progress.

This paper is based on observations made with ESO Telescopes at the Paranal Observatory under programme ID 083.B-0681(A) and the NASA/ESA Hubble Space Telescope (proposal ID 9289), obtained from the data archive at the Space Telescope Science Institute. STScI is operated by the Association of Universities for Research in Astronomy, Inc. under NASA contract NAS 5-26555. This work also used data obtained at the Gemini Observatory (proposal IDs GN-2001B-Q-10 & GN-2003B-DD-3), which is operated by the Association of Universities for Research in Astronomy, Inc., under a cooperative agreement with the NSF on behalf of the Gemini partnership: the National Science Foundation (United States), the Science and Technology Facilities Council (United Kingdom), the National Research Council (Canada), CONICYT (Chile), the Australian Research Council (Australia), Min-

istrio da Cincia, Tecnologia e Inovao (Brazil) and Ministerio de Ciencia, Tecnologia e Innovacion Productiva (Argentina).

REFERENCES

- Abazajian K. N., et al. 2009, *ApJS*, 182, 543
 Baum W. A., 1959, *PASP*, 71, 106
 Bender R., Surma P., Doebereiner S., Moellenhoff C. and Madejsky R., 1989, *A&A*, 217, 35
 Bender R., Burstein D. and Faber S. M., 1993, *ApJ*, 411, 153
 Beifiori A., Maraston C., Thomas D., and Johansson J., 2011, *A&A*, 531, A109
 Böhringer H., Briel U. G., Schwarz R. A., Voges W., Hartner G. and Trümper J., 1994, *Nature*, 368, 828
 Burstein D., Faber S. M., Gaskell C. M. and Krumm N., 1984, *ApJ*, 287, 586
 Cappellari M. and Emsellem E., 2004, *PASP*, 116, 138
 Cappellari M., et al., 2007, *MNRAS*, 379, 418
 Cappellari M., et al., 2011a, *MNRAS*, 413, 813
 Cappellari M., et al., 2011b, *MNRAS*, 416, 1680
 Corless V. L., King L. J. and Clowe D., 2009, *MNRAS*, 393, 1235
 de Vaucouleurs G., 1953, *MNRAS*, 113, 134
 Djorgovski S. and Davis M., 1987, *ApJ*, 313, 59
 Dressler A., 1980, *ApJ*, 236, 351
 Dressler A., Lynden-Bell D., Burstein D., Davies R. L., Faber S. M., Terlevich R. and Wegner G., 1987, *ApJ*, 313, 42
 Ebeling H., Voges W., Böhringer H., Edge A. C., Huchra J. P., and Briel U. C., 1996, *MNRAS*, 281, 799
 Emsellem E., et al., 2007, *MNRAS*, 379, 401
 Emsellem E., et al., 2011, *MNRAS*, 414, 818
 Gerhard O. E., 1993, *MNRAS*, 265, 213
 Halkola A., Seitz S., Pannella M., 2006, *MNRAS*, 372, 1425
 Houghton R. C. W., Davies R. L., Dalla Bontà E. and Masters R., 2012, *MNRAS*, 423, 256
 Komatsu E., et al., 2011, *ApJS*, 192, 18
 Krajnović D., Cappellari M., de Zeeuw P. T. and Copin Y., 2006, *MNRAS*, 366, 787
 Krajnović D., et al., 2011, *MNRAS*, 414, 2923
 Lemze D., Barkana R., Broadhurst T. J. and Rephaeli Y., 2008, *MNRAS*, 386, 1092
 Maraston C., 2005, *MNRAS*, 362, 799
 Oguri M., Takada M., Umetsu K. and Broadhurst T., 2005, *ApJ*, 632, 841
 Pasquini L., et al., 2002, *The Messenger*, 110, 1
 Prugniel, P. and Soubiran C., 2001, *A&A*, 369, 1048
 Sánchez-Blázquez P., et al. 2006, *MNRAS*, 371, 703
 Sandage A. and Visvanathan N., 1978, *ApJ*, 223, 707
 Sandage A. and Visvanathan N., 1978, *ApJ*, 225, 742
 Struble M. F. and Rood H. J., 1999, *ApJS*, 125, 35
 van der Marel R. P., Franx M., 1993, *ApJ*, 407, 525
 Visvanathan N. and Sandage A., 1977, *ApJ*, 216, 214
 Weijmans A.-M., et al., 2009, *MNRAS*, 398, 561
 de Zeeuw P. T., et al., 2002, *MNRAS*, 329, 513